JOURNAL OF ASIAN CERAMIC SOCIETIES
https://doi.org/10.1080/21870764.2022.2053278

FULL LENGTH ARTICLE

OPEN ACCESS Check for updates

# Macroporous bioceramic scaffolds based on tricalcium phosphates reinforced with silica: microstructural, mechanical, and biological evaluation

Lenka Novotna[a], Zdenek Chlup[b], Josef Jaros[c,d], Klara Castkova[a,e], Daniel Drdlik[a,e], Jakub Pospisil[c], Ales Hampl[c,d], Irena Koutna[c,f] and Jaroslav Cihlar[a,e]

[a]CEITEC - Central European Institute of Technology, Brno University of Technology, Brno, Czech Republic; [b]CEITEC - IPM, Academy of Sciences of the Czech Republic, Brno, Czech Republic; [c]Faculty of Medicine, Department of Histology and Embryology, Masaryk University, Brno, Czech Republic; [d]International Clinical Research Center - Center of Biomolecular and Cellular Engineering, St. Anne's University Hospital Brno, Brno, Czech Republic; [e]Faculty of mechanical engineering, Institute of Materials Science and Engineering, Brno University of Technology, Brno, Czech Republic; [f]International Clinical Research Center – Cell and Tissue Engineering facility, St. Anne's University Hospital Brno, Brno, Czech Republic

**ABSTRACT**

The positive effect of silica on microstructural, mechanical and biological properties of calcium phosphate scaffolds was investigated in this study. Scaffolds containing 3D interconnected spherical macropores with diameters in the range of 300–770 µm were prepared by the polymer replica technique. Reinforcement was achieved by incorporating 5 to 20 wt % of colloidal silica into the initial hydroxyapatite (HA) powder. The HA was fully decomposed into alpha and beta-tricalcium phosphate, and silica was transformed into cristobalite at 1200°C. Silica reinforced scaffolds exhibited compressive strength in the range of 0.3 to 30 MPa at the total porosity of 98–40%. At a nominal porosity of 75%, the compressive strength was doubled compared to scaffolds without silica. When immersed into a cultivation medium, the formation of an apatite layer on the surfaces of scaffolds indicated their bioactivity. The supportive effect of the silicon enriched scaffolds was examined using three different types of cells (human adipose-derived stromal cells, L929, and ARPE-19 cells). The cells firmly adhered to the surfaces of composite scaffolds with no sign of induced cell death. Scaffolds were non-cytotoxic and had good biocompatibility in vitro. They are promising candidates for therapeutic applications in regenerative medicine.

**ARTICLE HISTORY**
Received 21 December 2021
Accepted 11 March 2022

**KEYWORDS**
Bioceramics; scaffold; calcium phosphate; silica; compressive strength

## 1. Introduction

Nowadays, many people face problems related to bone disorders. Bone tissue is able to completely regenerate on its own if the damaged part is small enough. If not, it is necessary to heal such trauma, e.g. by using bone grafts. Autografts, i.e. parts of bone harvested from the patient's body, naturally have the most suitable properties, but some problems, such as lack of available tissue material and the necessity of multiple surgical procedures, were reported [1]. Nonetheless, because the bone is the second most common transplanted tissue, the demand for bone grafts is huge – several million people need them every year [2]. Hence, the development of a new type of synthetic graft, further referred to as a scaffold, seems to be a promising choice [3,4].

The requirements on the synthetic scaffolds are manifold [5,6]; the ideal scaffold must be biocompatible, i.e. must not elicit any inflammatory response and/or demonstrate immunogenicity or cytotoxicity. It should support tissue formation by 3D structures with pores allowing cells to migrate throughout the biomaterial scaffold and support vascularization of the ingrown tissue. Pores must be interconnected, with a pore size of minimally 100 µm in diameter (ideally >300 µm) [7,8]. Besides such macropores, the microporosity (<10 µm) of the struts is desirable because it provides a larger surface area, which is critical for protein adsorption, and adhesion and growth of cells [7,9]. Within few months the scaffold should resorb in the body environment. The resorption kinetics should ideally be equal to the bone turnover rate in order to facilitate load transfer directly to the newly developing bone. The by-products of the body-scaffold interaction must not be toxic and should be easy to eliminate via relevant body systems [10]. Also, mechanical properties should be similar to those of replaced bone, i.e. compressive strength of cancellous bone is in the range of approx. from 1 to 38 MPa [11–13], and the scaffold must not collapse during handling and in vivo during normal physical activities. Scaffolds should be easy to manufacture in shapes, which accurately fit the defects in the bone. Hence, the intrinsic structure, as well as the composition, play crucial roles in the clinical success of the scaffold.

**CONTACT** Daniel Drdlik daniel.drdlik@ceitec.vutbr.cz CEITEC - Central European Institute of Technology, Brno University of Technology, Purkynova 123, Brno 612 00, Czech Republic

Bioceramic materials based on calcium phosphates exhibit the greatest chemical similarity to the bone mineral component [14]. Their wide expansion into clinical practice is, however, limited by insufficient mechanical properties if they are prepared synthetically. The objective of this work was to develop a new composite biomaterial with biological characteristics and compressive strength similar to highly porous hard tissues. Silica was chosen as the reinforcing phase because silicon (as $Si^{4+}$ ion) is considered to be one of the essential trace elements required for the development of healthy bones. It acts as a biological cross-linking agent in the extracellular matrix. Moreover, it enhances osteoblast proliferation, differentiation, and collagen production [15,16]. Calcium phosphate ceramics substituted by silicate ions exhibit superior biological properties compared to their stoichiometric counterparts [17]. Up to now, a great deal of material research was focused on bioceramics containing amorphous silica such as bioactive glasses [18–21] (pseudo) wollastonite [22–25], dicalcium silicate [26] and Si-doped CaP [17,27–29].

On the other hand, materials composed of crystalline silica in the form of quartz or cristobalite for medical applications were poorly studied so far. There are only a few studies concerning bioactive composites composed of cristobalite and calcium phosphate matrix such as dicalcium phosphates [30,31], tetracalcium phosphate [32] or HA (reinforced with biogenic silica) [33]. Therefore, here we aimed to extend the knowledge on bioactive material composition based on silica – tricalcium phosphate (TCP/$SiO_2$), where the crystalline silica, in the form of cristobalite formed after sintering, plays a crucial role.

In this study, the TCP/ $SiO_2$ composite scaffolds were fabricated by the polymer replica technique. The silica content varied from 0 to 20 wt % and the effect of cristobalite, overall phase composition, sintering temperature, pore size, and total porosity on microstructural, mechanical and biological properties of tricalcium phosphate scaffolds were investigated.

## 2. Materials and methods

### 2.1. Ceramic foam processing

Ceramic scaffolds were prepared by the polymer replica technique. This method was chosen for the manufacturing of the bioceramic scaffolds because it accurately mimics a trabecular bone macrostructure. Polyurethane foam (PU) with initial pore sizes of 45, 60, 75 and 90 PPI (Bulpren S 28133, S 28089, S 31062, S 31048, Eurofoam, Czech Republic) were cut into cylinders of ø 7.5 × 10 mm (for a compressive test) and ø 5 × 2 mm (for biological testing). Subsequently, they were immersed into ceramic slurries containing HA with 0, 5, 10, 15 and 20 wt. % silica. Two types of slurries were prepared. A silica-free slurry (as a reference) was prepared from HA powder (purity >90%, Fluka, Switzerland) bonded by 5 wt % polyvinyl alcohol (PVA, Mowiol 10–98, Sigma Aldrich, Germany), deionized water, 0.2 wt % glycerol (Onex, Czech Republic) and 0.1 wt % n-octanol (Lachema, Czech Republic). The second type was prepared by mixing HA powder (purity > 90%, Fluka, Switzerland), colloidal silica solution LUDOX® SK-R (Grace, US) and deionized water. The weight fraction of HA in the slurry was in the range of 0.45 to 0.5. The coating process was repeated if a lower porosity of the scaffolds was required. Slurry residues were then gently removed from the surface of impregnated PU templates by compressed air to achieve the desired calculated porosity. The scaffolds prepared were dried at 25°C for 24 h. To burnout the PU template and achieve a sufficient manipulation strength the scaffolds were calcined at 1000°C with a heating rate of 1°C/min. The scaffolds were finally pressureless sintered in air at 1200°C for 3 h with a heating rate of 5°C/min and a cooling rate of 10°C/min.

### 2.2. Thermal, physical and structural characterization of scaffolds

Thermal analysis of the as-coated PU template was performed using a 6300 Seiko Instruments TG-DTA (Seiko Instruments, Japan). The specimen was measured at temperatures between 35 and 1000°C with a heating rate of 2°C/min in a mixture of air and argon (1:1); the flow rate was set to 400 ml/min.

The phase composition of HA and composites (5–20 wt % $SiO_2$) was determined via an X-ray powder diffractometer SmartLab 3 kW (XRD, Rigaku, Japan). The diffraction patterns were measured from 15° to 90° (2θ) with Cu Kα radiation. For this purpose, the sintered scaffolds were crushed into a fine powder which was subsequently analyzed. The phase content was quantified using the Rietveld analysis. The evaluation of the crystallographic structures and quantitative analyses were realized using the PDXL2 software.

The morphology of sintered scaffolds was observed using a scanning electron microscope (SEM, ZEISS Ultra Plus, Germany) equipped with an EDX analyzer (Oxford Instruments, UK). The scaffolds were embedded in a resin, ground and polished by the standard ceramographic methods. To quantify the pore sizes and their distribution, image analysis of SEM micrographs was done using the ImageJ software (National Institutes of Health, US).

The total porosity was calculated from the geometric volume, mass and theoretical density according to EN 623–2:1993:

$$P = \frac{\rho_t - \rho_b}{\rho_t} \times 100 \quad (1)$$

**Table 1.** Nominal ion concentrations (in mM) of MEM in comparison with SBF solution and human blood plasma [34,35].

| | $Na^+$ | $K^+$ | $Mg^{2+}$ | $Ca^{2+}$ | $Cl^-$ | $HCO_3^-$ | $HPO_4^{2-}$ | $SO_4^{2-}$ | pH |
|---|---|---|---|---|---|---|---|---|---|
| DMEM | 155.3 | 5.3 | 0.8 | 1.8 | 119.3 | 44 | 0.9 | 0.8 | 7.4 |
| MEM | 144.4 | 5.3 | 0.8 | 1.8 | 126.2 | 26.2 | 1.0 | 0.8 | 7.4 |
| SBF | 142.0 | 5.0 | 1.5 | 2.5 | 147.8 | 4.2 | 1.0 | 0.5 | 7.4 |
| Blood plasma | 142.0 | 5.0 | 1.5 | 1.5 | 103.0 | 27.0 | 1.0 | 0.5 | 7.2–7.4 |

where $\rho_t$ is the theoretical density and $\rho_b$ is the bulk density. The bulk density is defined as:

$$\rho_b = \frac{m_b}{V_b} \tag{2}$$

where $m_b$ is the mass of the dry test piece and $V_b$ is the total geometrical volume (the sum of the volumes of the solid material, the open and the closed pores). Additionally, the apparent density as the ratio between weight and geometrical volume for each analyzed scaffold prior to testing was individually calculated to allow a better understanding of the mechanical properties observed.

### 2.3. Mechanical testing – compressive strength of scaffolds

The compressive strength of prepared scaffolds was determined using an Instron 8862 electromechanically driven testing system (Instron, USA) of nominal capacity 100 kN and equipped with a 5 kN load cell and precise clip-gauge for the deformation measurement. Cylindrical scaffolds of nominal dimensions after sintering ø 6 mm × 8 mm were inserted between compressive platens with 1 mm thick leather spacers used for a proper load transfer from the steel platen to the scaffold. A cross-head speed of 0.5 mm/min was used for the loading. The compressive strength was calculated from the force corresponding with the first peak on the loading curve (force vs displacement) followed by a significant drop in applied force and scaffold dimensions. This approach leads to an estimate of the initial compressive strength of prepared scaffolds, which is important from the application point of view. Note that the determined strength here can be slightly lower than the "effective" compressive strength as determined from the plateau in the loading curve. A minimum of four scaffolds of the same pore size, porosity and composition were measured.

### 2.4. Evaluation of bioactivity of scaffolds

The bioactivity potential, i.e. the bone-bonding ability, was studied by means of apatite formation on the scaffold surfaces. Instead of the typically used simulated body fluid (SBF) prepared following the Kokubo recipe [34], the epitaxial growth of apatite was studied using Dulbecco's Modified Eagle Medium – DMEM (GE Healthcare, USA). It can be a better choice in terms of simulating the in vivo environment [35] because it contains, except the ionic composition like SBF (see Table 1), other components occurring in in vivo systems (such as glucose, amino acids and vitamins). The principle of bone-like apatite formation on scaffold surfaces is analogous to that in SBF solution and can be found elsewhere [35–37]. Scaffolds were incubated in the medium for 3 days at 37°C under a humidified atmosphere of 95% air and 5% $CO_2$. After the removal from the medium and rinsing with deionized water, the scaffolds were dried at 25°C. The presence of the apatite layer on the surface was examined using SEM.

### 2.5. Assaying biocompatibility in vitro: metabolic activity of cells

The viability and proliferation of cells on TCP and TCP/$SiO_2$ scaffolds were assessed *in vitro* by MTT assay. Cytotoxicity tests for scaffolds were performed according to the ISO 10993–5:2009(E) Biological evaluation of medical devices – Tests for *in vitro* cytotoxicity guidelines. Two standardized cell lines were used to determine the cytotoxicity of the materials: L929 cells (NCTC clone 929: CCL 1, LOT: 70026472, American Type Culture Collection [ATCC], Manassas, VA, USA), and more sensitive ARPE-19 cells (ARPE-19: CRL-2302, LOT: 70013110, American Type Culture Collection [ATCC], Manassas, VA, USA).

### 2.6. Assaying biocompatibility in vitro: morphology of cells growing on scaffolds

Scaffolds containing 0 and 10 wt % of silica were sterilized by UV-irradiation for 20 minutes in the flow box. Scaffolds were wet in DMEM-Glutamax (Life Technologies, Czech Republic) medium for 1 h and centrifuged for 10 min to eliminate air bubbles from the material.

Adipose-derived stromal cells (ADSCs) were isolated from adipose tissue by centrifugation and collagenase extraction, as described elsewhere [38]. Briefly, adipose tissue was digested with 0.1% collagenase type IV for 30 min at 37°C. After enzyme activity neutralization by DMEM-F12 (Life Technologies, Czech Republic) with 10% fetal bovine serum (FBS), cells were separated by centrifugation. The pellet was resuspended in cultivation medium (10% FBS, 0.5% penicillin/streptomycin

(GE Healthcare Life Sciences, USA) in DMEM Glutamax) and propagated on a culture dish coated with 0.01% gelatin. Subsequently, the cells were trypsinized and seeded on materials at a concentration of 50.000/100 µL for analysis of cell viability and 1 million cells/100 µL for evaluation of cell morphology. Scaffolds were analyzed after 24 h of cultivation.

Due to the similar composition of scaffolds, the cell viability was assessed on scaffolds with 75 PPI porosity by fluorescent live/dead assay. The fluorescent stock solution was prepared by diluting 0.03% w/v of acridine orange and 0.1% w/v of ethidium bromide (both Sigma-Aldrich, USA) into 2% ethanol in distilled water, with a final dilution of 1/1000 in 0.1 M phosphate buffer. The fluorescent solution was added to the specimens for 5 min 25°C and live/dead cells were visualized using an epifluorescence microscope Cell^R (Olympus C&S Ltd., Japan).

Cells cultivated for 24 h on tested specimens were fixed with 4% paraformaldehyde dissolved in 0.1 M phosphate buffer (PBS) and permeabilized by 0.1% Triton TX-100 (Merck, Germany). Actin cytoskeleton was stained with 60 nM Phalloidin Rhodamine (R415, Lifetech, Czech Republic) dissolved in 0.1 M PBS, and cell nuclei were stained with 1 µg/mL 4′,6-diamidino-2-phenylindole, (Sigma-Aldrich, USA). The specimens were observed by the epifluorescence microscope Cell^R (Olympus C&S Ltd., Japan).

## 3. Results and discussion

### 3.1. Thermal analysis

TGA curves of the PU foam template coated with HA powder reinforced with 10 wt % $SiO_2$ (the overall weight of the system with respect to PU is therefore as follows: PU (10 wt %), HA (81 wt %) and $SiO_2$ (9 wt %)) are given in Figure 1. The minimum weight loss (~1%) at temperatures from 40 to 200°C was caused mainly by the evaporation of adsorbed water. At temperatures between 200°C and 550°C, the two-stage thermal decomposition process of the PU foam template was observed. This decomposition behavior, typical of PUs, was described in various studies [39–43] as primarily a polymer splitting process that begins at about 200°C. At this temperature, hard segments (related to urethane links) start to decompose, while the second step of degradation (350–550°C) is caused by oxidation of soft segments (related to the ether group) [44]. The exothermic peak on the DTA curve (see Figure 1) in the same temperature range confirmed that the degradation process of the PU occurred by an oxidation mechanism.

Experimental data show that the weight loss of the specimen continued even above the temperature of 550°C, at which the PU was supposed to have already burnt out. This was likely caused by the thermal transformation of the HA powder. The endothermic drop on the DTA curve around 800°C was related to the thermal transformation of HA to hydroxyoxyapatite (HOA) [45].

The total weight loss of 15% below 1000°C corresponded to the initial amount of PU in the composite, adsorbed water and weight loss of commercial HA caused by the reaction of secondary phase – monetite (see Chapter 3.2).

### 3.2. Phase composition

X-ray diffraction (XRD) patterns of sintered scaffolds are shown in Figure 2. The commercial ceramic powder was composed of HA and monetite. The quantitative analysis showed about 13 wt % of monetite as can be seen in Table 2. In the first instance, the HA was thermally decomposed to HOA with the following decomposition to the TCP phase according to the following equations [45]:

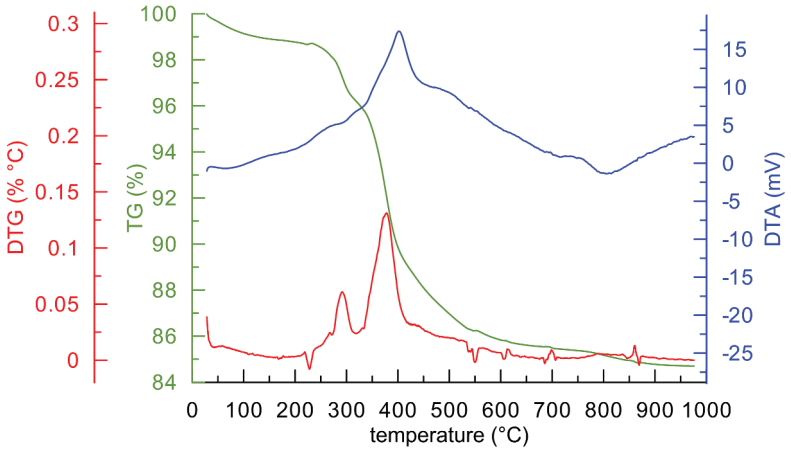


**Figure 1.** Thermogravimetric analysis of commercial reticulated polyurethane foam coated with HA powder reinforced with 10 wt % $SiO_2$.

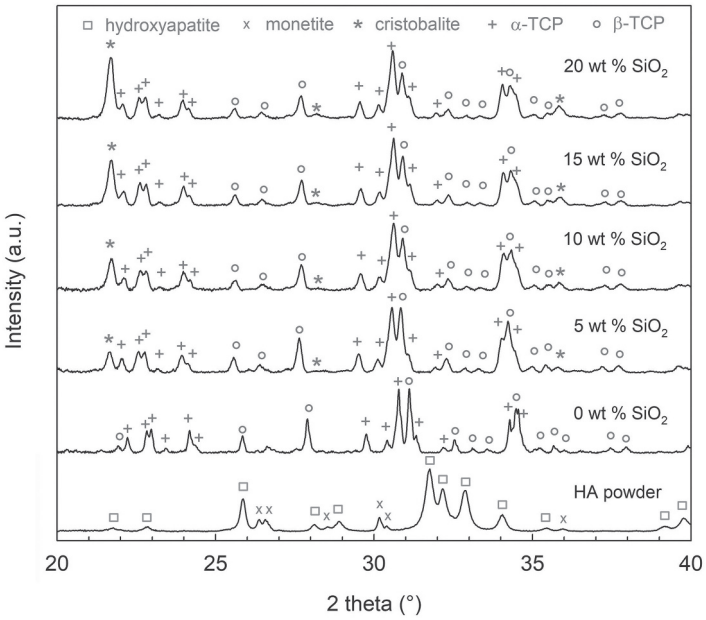


**Figure 2.** X-ray diffraction patterns of initial HA powder and TCP/$SiO_2$ composite scaffolds containing 0–20 wt % $SiO_2$, sintered at 1200°C for 3 h.

**Table 2.** Quantitative analysis results for initial ceramic powder and tricalcium phosphates reinforced with silica.

| Material (wt %) | powder | 0 wt % $SiO_2$ | 5 wt % $SiO_2$ | 10 wt % $SiO_2$ | 15 wt % $SiO_2$ | 20 wt % $SiO_2$ |
|---|---|---|---|---|---|---|
| hydroxyapatite | 87 | | | | | |
| monetite | 13 | | | | | |
| α-TCP | | 42 | 52 | 55 | 55 | 54 |
| β-TCP | | 58 | 44 | 37 | 33 | 29 |
| cristobalite | | | 4 | 8 | 12 | 17 |

$$2Ca_5(PO_4)_3OH \leftrightarrow Ca_{10}(PO_4)_6O_x(OH)_{2(1-x)} + xH_2O, 0 \leq x \leq 1 \quad (3)$$

$$Ca_{10}(PO_4)_6O_x(OH)_{2(1-x)} \leftrightarrow 3Ca_3(PO_4)_2 + CaO + (1-x)H_2O \quad (4)$$

The monetite phase was most likely decomposed during the sintering process to calcium pyrophosphate according to decomposition reaction [46]:

$$2CaHPO_4 \leftrightarrow Ca_2P_2O_7 + H_2O \quad (5)$$

Then the resulting calcium oxide and calcium pyrophosphate reacted to the TCP phase:

$$Ca_2P_2O_7 + CaO \leftrightarrow Ca_3(PO_4)_2 \quad (6)$$

Therefore, the original ceramic powder (without silica) was fully decomposed into α- and β-TCP in the scaffold after sintering at 1200°C (see Figure 2). In the literature, there is a vast discrepancy in the temperatures at which the decomposition of HA starts. According to many authors [47,48], HA should remain stable up to at least 1300°C. In our experiments (data are not shown here), a commercial HA started to decompose at about 800°C; almost half of the powder was transformed at 1000°C. This phenomenon can be attributed to the presence of impurities such as the monetite phase. Further increase in temperature led to the transformation of the β-TCP into the α–phase. Newly formed TCPs are believed to be more soluble in the body fluid than stoichiometric HA [49].

The phase composition of scaffolds containing silica was much more complex. Besides the α- and β- TCP, a new crystalline phase was formed after scaffold sintering. With increasing concentration of silica, the intensity of new strong diffraction at about 21.7° and two weak diffractions at about 28.2° and 35.8° increased and they were identified as cristobalite ($P4_1 2_1 2$ space group). The weight percentage of cristobalite within crystalline phases was roughly equivalent to the amount of colloidal silica in the initial slurry as documented by XRD quantitative analysis in Table 2.

The results of the XRD analysis also showed that the amount of the α and β TCP phases were almost equal in the absence of silica. However, the ratio between α-TCP and β-TCP significantly increased with the increasing amount of silica. The addition of silica significantly reduced the amount of β-TCP phase (from 58 to 29 wt %, see Table 2) whereas the α-TCP phase has been fixed at around 55 wt %. This behavior can be attributed to Si doping into α-TCP structure and formation of the most stable phase. Some studies [17,27,50] confirmed that the addition of silica shifts the temperature of HA→ α-TCP transformation to lower values. The stable α-TCP phase could be formed even during sintering above 700°C [17,27,28,50,51]. It was further reported that HA sintered in the presence of silica transformed to silica-substituted tricalcium phosphate (Si-α-TCP) with formula $Ca_3(P_{1-x}Si_xO_{4-x/2})_2$ [17,28] according to the following equation [50]

**Table 3.** Crystallographic parameters of pure and Si-substituted calcium phosphate phases.

| Phase | Lattice parameters | Space group | Ref. |
|---|---|---|---|
| measured α–TCP | a = 12.878 Å; b = 27.291 Å; c = 15.257 Å; β = 126.32° | $P2_1/a$ | – |
| measured Si–α–TCP (10 wt %) | a = 12.856 Å; b = 27.337 Å; c = 15.218 Å; β = 126.35° | $P2_1/a$ | – |
| measured β–TCP | a = b = 10.4263 Å; c = 37.423 Å | R3c | – |
| measured Si–β–TCP (10 wt %) | a = b = 10.4381 Å; c = 37.4933 Å | R3c | – |
| α–TCP | a = 12.887 Å; b = 27.280 Å; c = 15.219 Å; β = 126.20° | $P2_1/a$ | [52] |
| Si–α–TCP (0.87 wt % Si) | a = 12.875 Å; b = 27.372 Å; c = 15.225 Å; β = 126.30° | $P2_1/a$ | [28] |
| Si–TCP | a = 12.863 Å; b = 27.357 Å; c = 15.232 Å; β = 126.38° | $P2_1/a$ | [50] |
| β–TCP | a = b = 10.4352(2) Å; c = 37.4029(5) Å | R3c | [53] |

$$6Ca_5(PO_4)_3OH + 2SiO_2 \rightarrow 10Ca_3\left(P_{1-x}Si_xO_{4-x/2}\right)_2 + 3H_2O \quad (7)$$

Being of the same space group, the Si-substituted α-TCP can be distinguished from its stoichiometric counterpart by different lattice parameters [17,28]. Measured and theoretical (α-TCP [52], Si-α-TCP [28,50], β-TCP [53]) lattice parameters are compared in Table 3 (data shown for scaffold containing 10 wt % $SiO_2$). The obtained data of the lattice parameters (showing an increase of the b-axis length and β-angle) [27,28,54,55] indicate that our α-TCP was presumably substituted. Diffraction peak shifts of Si substituted TCP compared to undoped TCP confirm the lattice parameter changes, as also evident from Figure 2.

The shift of diffraction patterns to lower angles and change of the lattice parameter in c-axis (see Table 3) indicates that β-TCP might also have been silica-substituted. This partial substitution may have occurred by diffusion of silicate ions into the already transformed β-TCP phase. Nevertheless, further measurements are needed to confirm this assumption.

### 3.3. Characterization of structure and morphology of scaffolds

Ceramic scaffolds were prepared in a wide range of porosities and pore sizes. Porosity (40–98%) was easily tunable by the initial PPI of the PU template, by the viscosity of the slurry, by repeating the coating process and, finally, by the efficiency of removing the extra slurry by compressed air. If the total porosity was lower than 50%, the macropores were almost closed and the remaining pores were too small for efficient cell ingrowth. According to the Jodati review [56] an optimal porosity for osteogenesis appeared to be approximately 60%. In our case, the porosity seemed to be ideal in the range of 65–80% as regards the scaffold morphology (interconnected macropores) and strength. If the porosity exceeded 90%, the PU template was almost perfectly replicated, but such scaffolds were fragile with no sufficient manipulation strength due to very thin struts.

**Table 4.** Pore sizes of the fabricated scaffolds.

| | Pore size (μm) | | | |
|---|---|---|---|---|
| Scaffold | 45 PPI | 60 PPI | 75 PPI | 90 PPI |
| 0 wt % $SiO_2$ | 710 ± 65 | 550 ± 70 | 540 ± 60 | 330 ± 30 |
| 5 wt % $SiO_2$ | 715 ± 70 | 450 ± 30 | 420 ± 40 | 300 ± 30 |
| 10 wt % $SiO_2$ | 720 ± 70 | 470 ± 30 | 440 ± 30 | 310 ± 30 |
| 15 wt % $SiO_2$ | 725 ± 80 | 480 ± 20 | 450 ± 30 | 315 ± 30 |
| 20 wt % $SiO_2$ | 770 ± 50 | 525 ± 30 | 490 ± 30 | 350 ± 30 |

An overview of the macropore sizes of scaffolds reinforced with 10 wt % $SiO_2$ prepared from PU foam templates with initial pore sizes of 45 PPI, 60 PPI, 75 PPI, and 90 PPI and having 75% porosity is shown in Table 4 and Figure 3. The pore size of sintered scaffolds was dependent on the initial pore size of the PU foam template, the thickness of the struts and shrinkage during their sintering. The most convenient pore size for the applications in tissue engineering, i.e. from 150 to 500 μm [9,57], was observed for scaffolds prepared from the PU templates having a porosity of 60 to 90 PPI, where the measured pore size was in the range from 300 to 550 μm. Such range is ideal for cell migration as it was also reported in the work of Karageorgiou et al. [7].

In terms of the microstructure of struts, the differences between individual compositions were more significant (see Figure 4). Pure TCP scaffolds exhibited high microporosity in the struts (based on their low density <65 vol %) and overall higher geometrical dimensions (lower shrinkage) indicating insufficient particle packing during processing and sintering. The scaffolds containing silica had noticeably lower

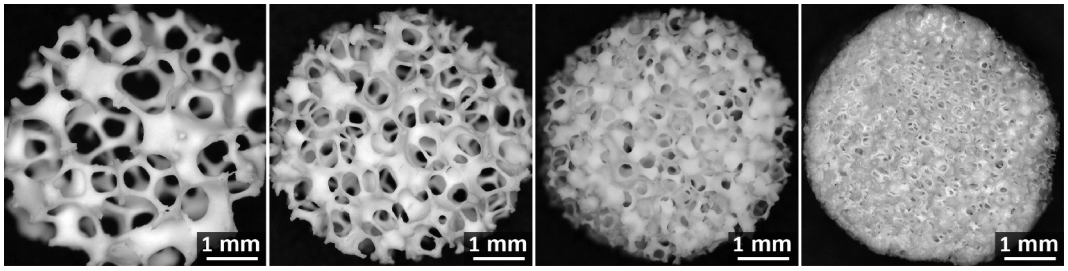


**Figure 3.** Macrostructure of TCP/$SiO_2$ composite scaffold (10 wt % $SiO_2$) having 75 vol % porosity sintered at 1200°C/3 h; pore sizes of the PU foam template from left to right: 45 PPI, 60 PPI, 75 PPI, and 90 PPI.

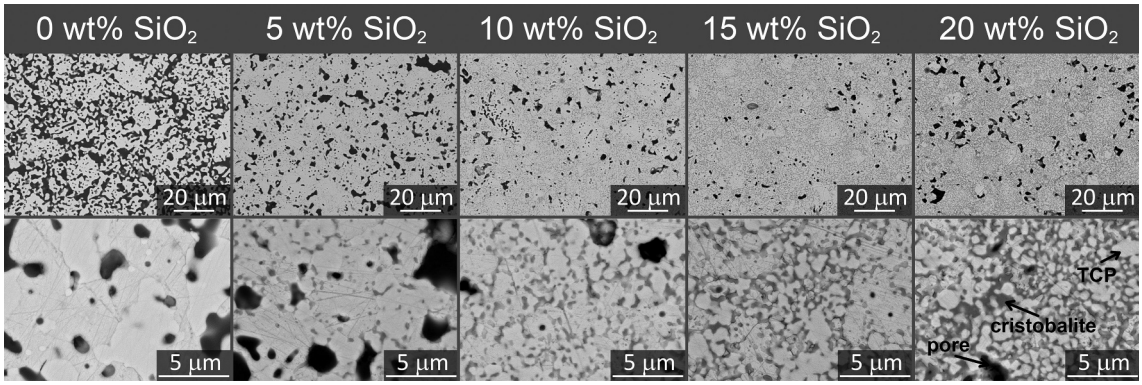


**Figure 4.** SEM cross-section micrographs of struts in scaffolds (top row – overall overview, bottom row – detailed images at higher magnification). Individual phases are marked by arrows (white areas – TCP, gray areas – cristobalite, black areas – micropores).

microporosity in the struts. This can be attributed to colloidal silica particles, which filled the spaces between HA particles and transformed into the cristobalite during processing and sintering. Its amount (the darker area) in Figure 4 grew proportionally with increasing initial silica content. For the lowest silica content, it was located in small areas near the grain boundaries. With increasing silica concentration, it formed a continuous network around the TCP grains. The grains were smaller in the presence of silica; probably due to the grain boundary pinning effect when a low concentration of silica was present or suppressed diffusion at higher concentrations of silica. The micropores were open and interconnected in all tested scaffolds. The size of the micropores in the struts varied between 0.5 and 20 µm. Microporosity can negatively influence mechanical properties, but it is essential for protein adhesion, cell migration, and osseointegration [58,59].

### 3.4. Mechanical properties

The influence of the concentration of silica, i.e. presence of the cristobalite in the microstructure, on the compressive strength, was evaluated for scaffolds of various PU template pore sizes (45, 60, 75 and 90 PPI). The results are summarized in Figure 5. The comparison of dependence of compressive strength of pure TCP and TCP/$SiO_2$ composites on their total porosity is presented. Not surprisingly, the compressive strength increased exponentially with decreasing porosity by two orders of magnitude from 0.3 MPa to almost 30 MPa. The shift in the composite strength (gray symbols) to higher values compared with the pure TCP foams (white symbols) for the same densities is distinguishable, reaching more than threefold enhancement; however, the scatter of compressive strength values is significant. Such difference can be attributed to the presence of cristobalite in the microstructure (see Figures 2 and 4). It was reported that the cristobalite present in the tough matrix rather deteriorate mechanical properties [60]. The opposite phenomenon

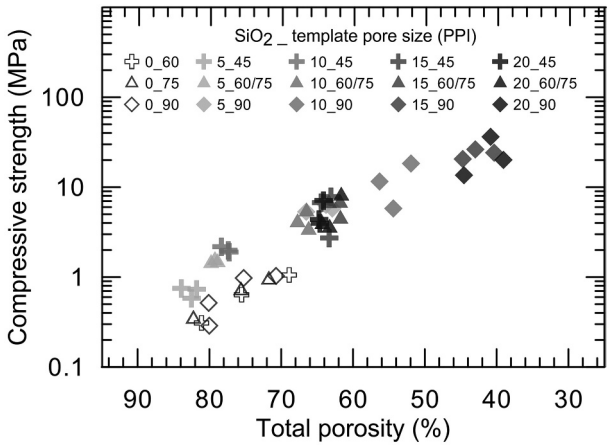


**Figure 5.** Dependence of compressive strength on total porosity for TCP and TCP/$SiO_2$ composite scaffolds.

occurs in a relatively mechanically weak matrix. Ansari et al. [61] reported a more than threefold increase in tensile strength for 20 vol % of cristobalite in hydroxyl-terminated polydimethylsiloxane. In the work of Li et al. [62], the cristobalite enhanced the compressive strength of geothermal geopolymer. However, the detail information about the influence of cristobalite on the mechanical properties of ceramic materials is still poorly discussed in the literature. Generally, in the case of ceramics, especially hydroxyapatite or tricalcium phosphate, a certain amount of glassy phase may be advantageous, since the glass is expected to have a positive effect on the sintering behavior, densification and mechanical properties of the composite with respect to the original bioceramics [63]. Our results support this statement.

Due to the elimination of the influence of the total porosity (as a parameter having the most significant effect) on the compressive strength, a new set of scaffolds having the same porosity were prepared. A detailed view of the influence of the microstructure composition and the template pore size on the compressive strength of the optimized scaffolds at a nominal porosity of approximately 75% is given in Figure 6. The trend in the obtained data is reaching the

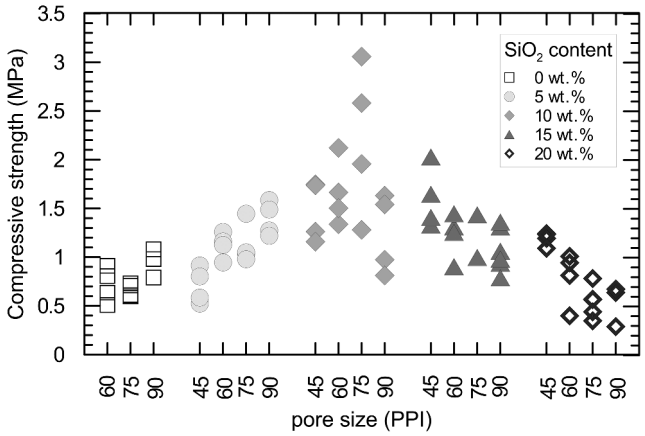


**Figure 6.** Compressive strength at 75% porosity for TCP and TCP/$SiO_2$ composite scaffolds prepared from initial PU foam templates with pore sizes: 45 PPI, 60 PPI, 75 PPI, and 90 PPI.

maximum (in the range of 1–3 MPa) for scaffolds having initially 10 wt % content of silica and a typical macropore size of 440 µm. A similar limit was reported by Oktar and Göller [64] for a glass-reinforced HA. A closer look at each material composition suggests that smaller initial pores resulted in higher compressive strength. However, this behavior takes place up to the initial 10 wt % content of silica. The opposite trend was observed for scaffolds containing 15 and 20 wt % of silica. From the mechanical strength point of view, the porosity was significantly reduced by the $SiO_2$ addition to the concentration of 10 wt % silica offering the best ratio between reduced overall porosity in the struts and only isolated cristobalite structure, as can be seen in Figure 4. This explains the maximum strength achieved. Since the higher concentration of the initial silica (15 and 20 wt %) in the scaffold led to the formation of the cristobalite interconnected network around the TCP grains, the scaffolds became more brittle.

One of the requirements imposed on the materials used in tissue engineering are properties similar to those of replaced tissues. The reported compressive strength of cancellous bone lays between 1.5 and 38 MPa [13], typically 2–20 MPa [12]. Therefore, the strength-porosity relationship of TCP/$SiO_2$ scaffolds indicates that the optimal strength for the bone tissue replacement can be reached using an optimized preparation method with 10 wt % of silica, as was demonstrated here.

### 3.5. Biological properties – bioactivity assessment in Dulbecco's Modified Eagle Medium

The bioactivity of prepared scaffolds was evaluated using the immersion test in a DMEM. Figure 7 presents an overview of the surface morphology of the scaffolds before and after soaking in the medium. After 3 days, almost the entire surface of scaffolds was covered with a newly formed apatite layer. This layer, nucleated

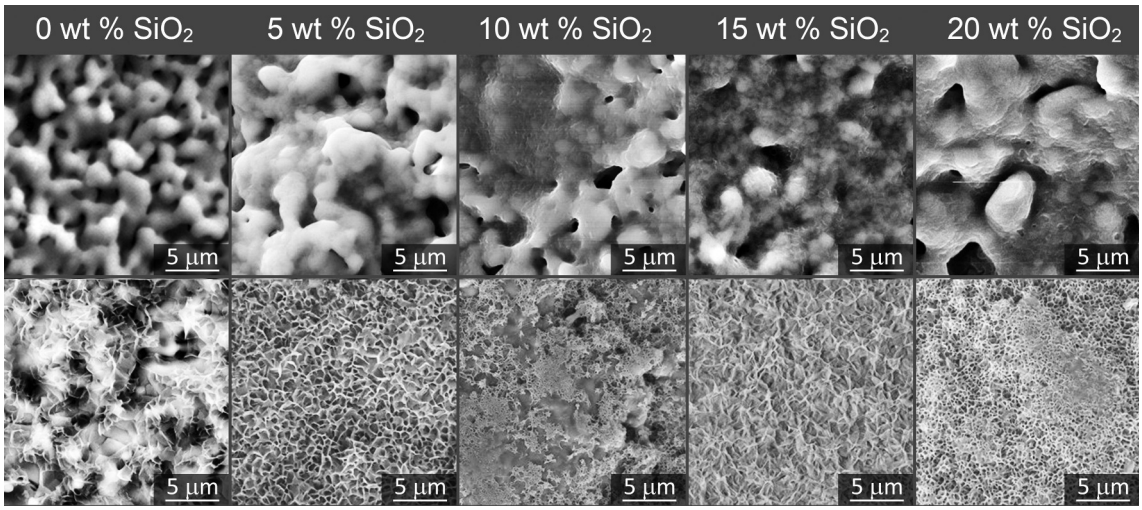


**Figure 7.** Surfaces of TCP and TCP/$SiO_2$ composite scaffolds before and after 3-day incubation in MEM.

under in-vivo-simulated conditions, indicates good bioactivity, i.e. bone-bonding ability, of all prepared scaffolds.

According to the literature [17,65–67], silica incorporated into the ceramic structure containing calcium phosphates can enhance the biomimetic precipitation on the surface of specimens immersed in the simulated body fluid. This can happen by two mechanisms. First, silicon can promote biomimetic precipitation on Si-α-TCP by the higher solubility of the material due to defects in the lattice [17,68,69]. Second, the higher biological activity can be influenced by the surface charge, which is here negative due to the substitution of $SiO_4^{4-}$ for $PO_4^{3-}$ ions, and can facilitate surface adhesion leading to the rapid biomimetic precipitation [17,70]. The bioactive behavior of some types of silicon-based ceramics was described in numerous studies [17,25,71,72].

### 3.6. Biological properties – metabolic activity of cells

The potential cytotoxicity of TCP and TCP/$SiO_2$ scaffolds of different pore sizes were assessed *in vitro* by MTT assay. MTT test is routinely used for measurement of viability and proliferation of standardized cell lines *in vitro* by colorimetric assessment of the metabolic activity of the cells. Figure 8 shows the MTT assay results for scaffolds of three different pore sizes (60, 75 and 90 PPI) containing 0 and 10 wt % of silica. As it is evident from the scaffold interactions with cells of both lines L929 and ARPE-1 (see Figure 8), all scaffolds indicated similar or higher cell viability compared to cells growing under standard 2D conditions. The results further revealed that neither composition nor pore size had significant effect on the cell viability. The viability of all tested samples was above the 70% viability threshold and within a 15% standard deviation range from the negative control. That means that no tested scaffold has proven any cytotoxic potential.

### 3.7. Biological properties – morphology of cells growing on scaffolds

Human ADSCs were seeded into calcium phosphate scaffolds to further test capability of material to support cell growth. These cells are well suited for analyzing clinically relevant cell–material interaction because of their human origin, non-cancerous nature, and multilineage differentiation potential. At 24 hours after seeding, majority of cells on all specimens exhibited green fluorescence signal, indicating their viability, with only few cells (less than 1%) being dying/dead, as demonstrated by red fluorescence signal. Such proportions are typical for *in vitro* cultured cells, so that ADSCs obviously did not undergo extensive material-induced cell death. Such finding was typical for all the materials examined here (TCP and TCP/$SiO_2$ with 10 wt % of silica) (see Figure 9).

Besides viability, morphological features of ADSCs have been also studied to evaluate behavior of cells growing on calcium phosphate scaffolds. As determined by visualizing nuclei and cytoskeletal elements, the cells adhered and became evenly distributed on internal surfaces of the scaffolds, with fully respecting details of scaffold morphologies. The cells grew in monolayer similarly to standard 2D culture in Petri dish, with producing

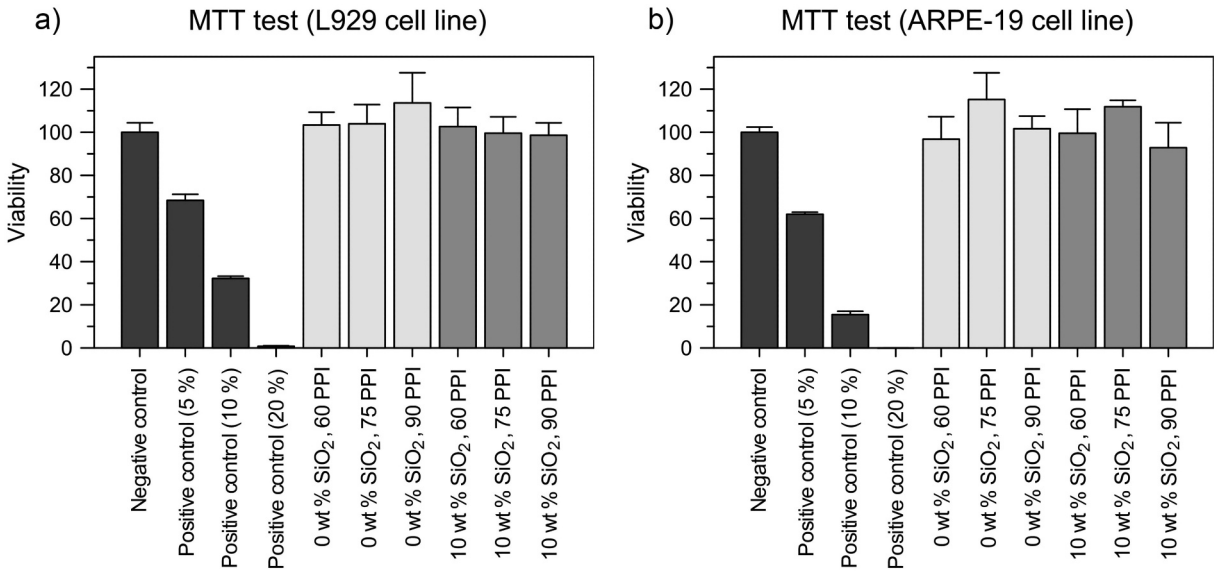


**Figure 8.** Relative viability of tested cell lines ((a) L929 cell line; (b) ARPE-19 cell line) when compared to the non-treated negative control cells. Positive controls were treated with medium with added DMSO (percentage values in brackets refer to percentage of DMSO in medium). Viability of all tested samples was above the 70% viability threshold and within 15% standard deviation range from the negative control. No tested sample have proven any cytotoxic potential.

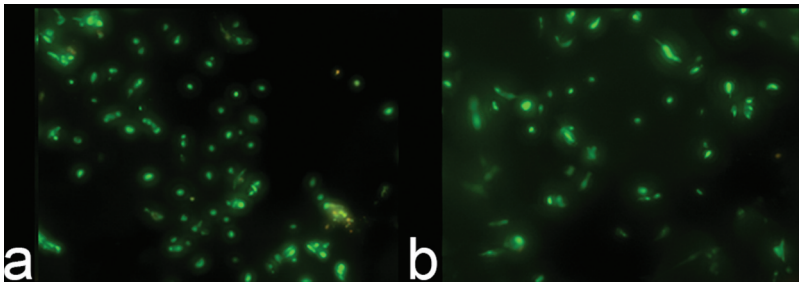


**Figure 9.** Cell viability assessment after 24 hours of cultivation. Cells seeded on scaffolds exhibited green fluorescence, indicating viable cells (merged images of red and green fluorescence) for both materials: (a) TCP, and (b) TCP/$SiO_2$ composite scaffold (10 wt % $SiO_2$).

protrusions (filopodia) in some parts of scaffolds. These protrusions, indicating active interaction with materials, were mainly detected on scaffolds with larger pores (45 and 75 PPI), as marked in the figures by white arrows (see Figures 10 and 11). It is of note that filopodia were more frequently seen in TCP/$SiO_2$ materials; further analyses of cell behavior (e.g. proliferation and formation of focal adhesion) should be performed for more detailed characterization.

Another significant phenomenon was penetration of cells through the pores and forming cell sheets, typically seen in the scaffolds with small pores (porosity 90 PPI, both TCP and TCP/$SiO_2$, green arrows in Figure 10. Also importantly, the cells were void of blebbing of their cytoplasmic membranes, and they had regularly shaped nuclei and well-developed network of actin, underlying their vital contacts with the supporting scaffold.

From the above described findings made using ADSCs, we conclude that our newly developed materials have no adverse effects on normal human cells, and instead they behave highly supportive so that they may represent a proper technological step toward clinical application.

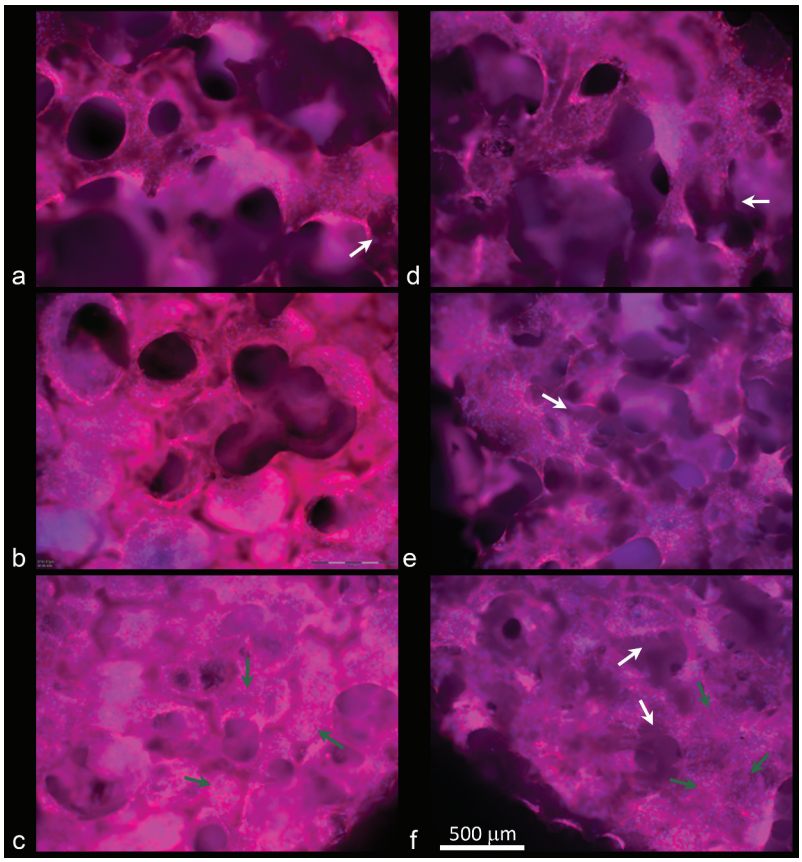


**Figure 10.** Morphological features of the cells grown in TCP scaffolds with initial porosity of (a) 45 PPI, (b) 75 PPI, (c) 90 PPI, and TCP/$SiO_2$ (10 wt % $SiO_2$) composite scaffolds with initial porosity of (d) 45 PPI, (e) 75 PPI, and (f) 90 PPI. Red color stains the actin and the blue visualizes the chromatin. White arrows indicate the formation of filopodia, green arrows indicate cells forming sheets over the scaffold pores.

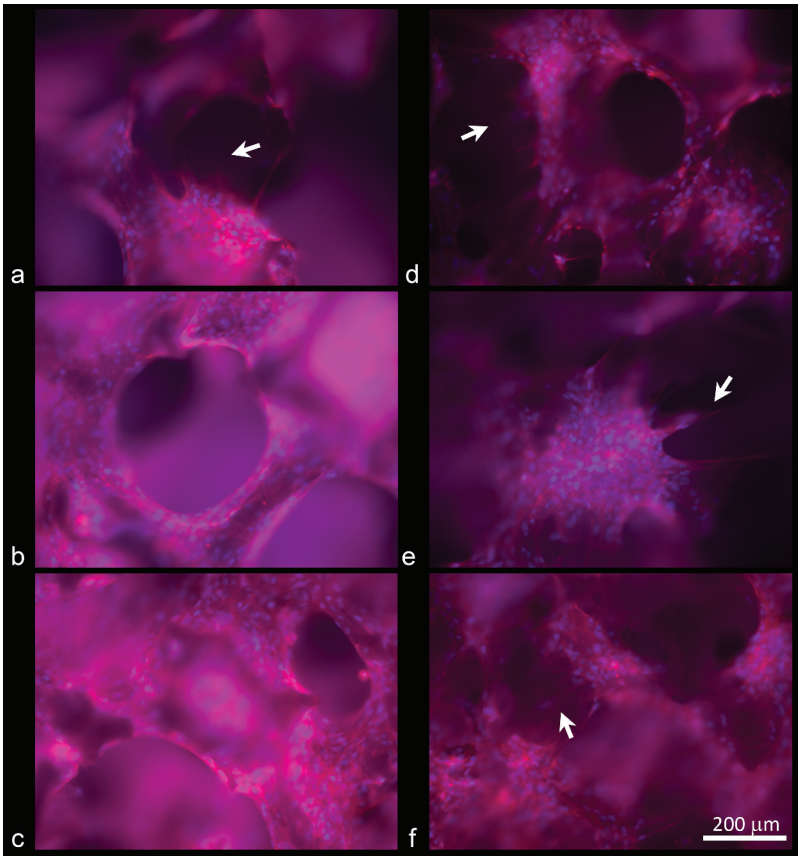


**Figure 11.** Detail representation of cellular adhesion and spreading of adipose-derived stromal cells on TCP scaffolds with initial porosity of (a) 45 PPI, (b) 75 PPI, (c) 90 PPI, and TCP/$SiO_2$ (10 wt % $SiO_2$) composite scaffolds with initial porosity of (d) 45 PPI, (e) 75 PPI, and (f) 90 PPI. White arrows indicate the formation of filopodia.

## 4. Conclusions

In this work, scaffolds based on calcium phosphates were prepared by the polymer replica technique. The pure and silica-rich (5–20 wt %) scaffolds with a 3D interconnected porosity (40–98%) were fabricated by templating the polyurethane foam with initial pore sizes of 45, 60, 75 and 90 PPI. The XRD analysis showed the total decomposition of the HA into α-TCP and β-TCP after sintering. Also, the strong diffraction of cristobalite was measured with an increasing concentration of silica in original scaffolds. It was proved that the silica significantly contributed to the phase transformation of HA to α-TCP. Moreover, the obtained data of the lattice parameters indicate that α-TCP had presumably been substituted by Si ions. Macropore dimensions of sintered scaffolds (between 300 and 770 µm) were dependent on the pore size of replicated templates. The measured average pore size of 300–550 µm in scaffolds prepared from the PU templates having a 60 to 90 PPI porosity was considered ideal for cells penetration based on available literature data. In terms of the struts microstructure, the scaffolds containing cristobalite had a noticeably higher density of struts with micropores in the range of 0.5 to 20 µm, which is essential for protein adhesion, cell migration and osseointegration. The compressive strength increased exponentially with decreasing porosity by two orders of magnitude from 0.3 MPa to almost 30 MPa. The presence of cristobalite in the composite scaffold structure led to a twofold increase in the compressive strength (1–3 MPa) compared to pure calcium phosphate scaffolds at a nominal porosity of 75%, which is in the range of the cancellous bone. The presence of cristobalite in the structure after sintering did not negatively affect the biological properties of scaffolds. *In vitro* tests demonstrated that all the scaffolds prepared were bioactive, as evidenced by the formation of an apatite layer on the surface after 72 h immersion in the medium. The scaffolds containing 0 and 10 wt % silica were not cytotoxic as demonstrated by MTT assay. The content of 10 wt % silica may even be beneficial to cells as it was indicated by cell viability assay using adipose-derived stromal cells. Such beneficial effect was maximally pronounced in materials with the smallest pores (90 PPI). Overall morphology of adipose-derived stromal cells growing on materials confirmed their proper supportive action.

Collectively, concerning phase composition, microstructure, compressive strength and biological properties, the promising candidates for potential application

in bone tissue engineering are TCP/$SiO_2$ scaffolds having 60–80 vol % porosity.

## Acknowledgments

This work was supported by the Ministry of Education, Youth and Sports under Grant COST LD14072; Czech Health Research Council under Grant NU20-08-00402; Ministry of Education, Youth and Sports under Grant CZ.02.1.01/0.0/0.0/16_026/0008451; Czech Science Foundation under Grant GA18-05510S; Ministry of Education, Youth and Sports under Grant CZ.02.1.01/0.0/0.0/15_003/0000492 and Ministry of Education, Youth and Sports under Grant LM2018110.

## Disclosure statement

No potential conflict of interest was reported by the author(s).

## Funding

This work was supported by the Agentura Pro Zdravotnický Výzkum České Republiky [NU20-08-00402]; Ministerstvo Školství, Mládeže a Tělovýchovy [LM2018110]; Grantová Agentura České Republiky [GA18-05510S]; Ministerstvo Školství, Mládeže a Tělovýchovy [CZ.02.1.01/0.0/0.0/15_003/0000492]; Ministerstvo Školství, Mládeže a Tělovýchovy [LD14072]; Ministerstvo Školství, Mládeže a Tělovýchovy [CZ.02.1.01/0.0/0.0/16_026/0008451].

## ORCID

Zdenek Chlup http://orcid.org/0000-0002-6117-240X
Daniel Drdlik http://orcid.org/0000-0003-4545-7779

## References

[1] Giannoudis PV, Dinopoulos H, Tsiridis E. Bone substitutes: an update. Injury. 2005 Nov;36 Suppl 3(3):S20–7.
[2] Bohner M. Resorbable biomaterials as bone graft substitutes. Mater Today. 2010;13(1–2):24–30.
[3] Hannink G, Arts JJ. Bioresorbability, porosity and mechanical strength of bone substitutes: what is optimal for bone regeneration? Injury. 2011 Sep;42 Suppl 2:S22–5.
[4] Giannoudis PV, Chris Arts JJ, Schmidmaier G, et al. What should be the characteristics of the ideal bone graft substitute? Injury. 2011;42:S1–S2.
[5] Jones JR, Boccaccini AR. Biomedical applications: tissue engineering. Cellular Ceramics: Wiley-VCH Verlag GmbH & Co. KGaA; 2006. p. 547–570.
[6] Roseti L, Parisi V, Petretta M, et al. Scaffolds for bone tissue engineering: state of the art and new perspectives. Mater Sci Eng C Mater Biol Appl. 2017 Sep 1;78:1246–1262.
[7] Karageorgiou V, Kaplan D. Porosity of 3D biomaterial scaffolds and osteogenesis. Biomaterials. 2005 Sep;26(27):5474–5491.
[8] Perez RA, Mestres G. Role of pore size and morphology in musculo-skeletal tissue regeneration. Mater Sci Eng C Mater Biol Appl. 2016 Apr 1;61:922–939.
[9] Liu Y, Lim J, Teoh SH. Review: development of clinically relevant scaffolds for vascularised bone tissue engineering. Biotechnol Adv. 2013 Sep-Oct;31(5):688–705.
[10] Hutmacher DW. Scaffolds in tissue engineering bone and cartilage. Biomaterials. 2000;21(24):2529–2543.
[11] Carter DR, Hayes WC. Bone compressive strength: the influence of density and strain rate. Science. 1976;194(1):174–1176.
[12] Olszta MJ, Cheng X, Jee SS, et al. Bone structure and formation: a new perspective. Mater Sci Eng R Rep. 2007;58(3–5):77–116.
[13] Alessandro R, Brucato V, Rimondini L, et al. I materiali biocompatibili per la medicina [Biomaterials for medicine]. Palermo: Atti del Convegno Nazionale della Società Italiana Biomateriali; 2014. Italian. p 15–18.
[14] Lei C, Cao Y, Hosseinpour S, et al. Hierarchical dual-porous hydroxyapatite doped dendritic mesoporous silica nanoparticles based scaffolds promote osteogenesis in vitro and in vivo. Nano Res. 2020;14(3):770–777.
[15] Nikom J, Charoonpatrapong-Panyayong K, Kedjarune-Leggat U, et al. 3D interconnected porous HA scaffolds with SiO2 additions: effect of SiO2 content and macropore size on the viability of human osteoblast cells. J Biomed Mater Res A. 2013 Aug;101(8):2295–2305.
[16] Lodoso-Torrecilla I, Klein Gunnewiek R, Grosfeld EC, et al. Bioinorganic supplementation of calcium phosphate-based bone substitutes to improve in vivo performance: a systematic review and meta-analysis of animal studies. Biomater Sci. 2020 Sep 7;8(17):4792–4809.
[17] Pietak AM, Reid JW, Stott MJ, et al. Silicon substitution in the calcium phosphate bioceramics. Biomaterials. 2007 Oct;28(28):4023–4032.
[18] Hench LL. Chronology of bioactive glass development and clinical applications. New J Glass Ceram. 2013;03(2):67–73.
[19] Jones JR. Review of bioactive glass: from Hench to hybrids. Acta Biomater. 2013 Jan;9(1):4457–4486.
[20] Baino F. Bioactive glasses – when glass science and technology meet regenerative medicine. Ceram Int. 2018;44(13):14953–14966.
[21] Łączka M, Cholewa-Kowalska K, Osyczka AM. Bioactivity and osteoinductivity of glasses and glass-ceramics and their material determinants. Ceram Int. 2016;42(13):14313–14325.
[22] Kunjalukkal Padmanabhan S, Gervaso F, Carrozzo M, et al. Wollastonite/hydroxyapatite scaffolds with improved mechanical, bioactive and biodegradable properties for bone tissue engineering. Ceram Int. 2013;39(1):619–627.
[23] Soares VO, Daguano JKMB, Lombello CB, et al. New sintered wollastonite glass-ceramic for biomedical applications. Ceram Int. 2018;44(16):20019–20027.
[24] Amin AMM, El-Amir AAM, Karunakaran G, et al. In-vitro evaluation of wollastonite nanopowder produced by a facile process using cheap precursors for biomedical applications. Ceram Int. 2021 Jul 1;47(13):18684–18692.
[25] De Aza PN, Luklinska ZB, Martinez A, et al. Morphological and structural study of pseudowollastonite implants in bone. J Microsc. 2000;197(1):60–67.
[26] Dai Y, Liu H, Liu B, et al. Porous β-Ca2SiO4 ceramic scaffolds for bone tissue engineering: in vitro and in vivo characterization. Ceram Int. 2015;41(4):5894–5902.
[27] Reid JW, Pietak A, Sayer M, et al. Phase formation and evolution in the silicon substituted tricalcium phosphate/apatite system. Biomaterials. 2005 6/; 26(16):2887–2897.

[28] Reid JW, Tuck L, Sayer M, et al. Synthesis and characterization of single-phase silicon-substituted alpha-tricalcium phosphate. Biomaterials. 2006 May;27(15):2916–2925.
[29] Mastrogiacomo M, Corsi A, Francioso E, et al. Reconstruction of extensive long bone defects in sheep using resorbable bioceramics based on silicon stabilized tricalcium phosphate. Tissue Eng. 2006 May;12(5):1261–1273.
[30] El-Ghannam AR. Advanced bioceramic composite for bone tissue engineering: design principles and structure-bioactivity relationship. J Biomed Mater Res A. 2004 Jun 1;69(3):490–501.
[31] Ming C, Greish Y, El-Ghannam A. Crystallization behavior of silica-calcium phosphate biocomposites: XRD and FTIR studies. J Mater Sci. 2004;15(11):1227–1235.
[32] Hesaraki S, Alizadeh M, Borhan S, et al. Polymerizable nanoparticulate silica-reinforced calcium phosphate bone cement. J Biomed Mater Res Part B Appl Biomater. 2012 Aug;100(6):1627–1635.
[33] Ribeiro SBN, da Veiga Junior VF, de Campos JB, et al. Influences of biosilica content from Amazonian freshwater sponge on calcium phosphates. J Aust Ceram Soc. 2021 2021 February 01;57(1):55–65.
[34] Kokubo T, Takadama H. How useful is SBF in predicting in vivo bone bioactivity? Biomaterials. 2006;27 (15):2907–2915.
[35] Lee JT, Leng Y, Chow KL, et al. Cell culture medium as an alternative to conventional simulated body fluid. Acta Biomater. 2011 Jun;7(6):2615–2622.
[36] Rohanová D, Boccaccini AR, Horkavcová D, et al. Is non-buffered DMEM solution a suitable medium for in vitro bioactivity tests? J Mater Chem B. 2014;2 (31):5068–5076.
[37] Tas AC. The use of physiological solutions or media in calcium phosphate synthesis and processing. Acta Biomater. 2014 May;10(5):1771–1792.
[38] Streit L, Jaros J, Sedlakova V, et al. A comprehensive in vitro comparison of preparation techniques for fat grafting. Plast Reconstr Surg. 2017;139(3): 670e–682e.
[39] Ravey M, Pearce EM. Flexible polyurethane foam. I. Thermal decomposition of a polyether-based, water-blown commercial type of flexible polyurethane foam. J Appl Polym Sci. 1997;63(1):47–74.
[40] Chattopadhyay DK, Webster DC. Thermal stability and flame retardancy of polyurethanes. Prog Polym Sci. 2009;34(10):1068–1133.
[41] Levchik SV, Weil ED. Thermal decomposition, combustion and fire-retardancy of polyurethanes—a review of the recent literature. Poly Int. 2004;53(11):1585–1610.
[42] Bilbao R, Mastral JF, Ceamanos J, et al. Kinetics of the thermal decomposition of polyurethane foams in nitrogen and air atmospheres. J Anal Appl Pyrolysis. 1996;37(1):69–82.
[43] Cakic S, Lacnjevac C, Rajkovic M, et al. Reticulation of aqueous polyurethane systems controlled by DSC method. Sensors. 2006 May;6(5):536.
[44] Cangemi JM, Claro Neto S, Chierice GO, et al. Study of the biodegradation of a polymer derived from castor oil by scanning electron microscopy, thermogravimetry and infrared spectroscopy. Polímeros. 2006;16 (2):129–135.
[45] Cihlář J, Buchal A, Trunec M. Kinetics of thermal decomposition of hydroxyapatite bioceramics.J Mater Sci. 1999 1999 December 01;34(24):6121–6131.
[46] Mulongo-Masamba R, El Kassri T, Khachani M, et al. Synthesis and thermal dehydroxylation kinetic of anhydrous calcium phosphate monetite CaHPO4. J Therm Anal Calorim. 2016 2016 April 01;124 (1):171–180.
[47] Muralithran G, Ramesh S. The effects of sintering temperature on the properties of hydroxyapatite. Ceram Int. 2000;26(2):221–230.
[48] Ramesh S, Tan CY, Tolouei R, et al. Sintering behavior of hydroxyapatite prepared from different routes. Mater Des. 2012;34:148–154.
[49] Samavedi S, Whittington AR, Goldstein AS. Calcium phosphate ceramics in bone tissue engineering: a review of properties and their influence on cell behavior. Acta Biomater. 2013 Sep;9(9):8037–8045.
[50] Sayer M, Stratilatov A, Reid J, et al. Structure and composition of silicon-stabilized tricalcium phosphate. Biomaterials. 2003 Feb;24(3):369–382.
[51] Langstaff S, Sayer M, Smith T, et al. Resorbable bioceramics based on stabilized calcium phosphates. Part I: rational design, sample preparation and material characterization. Biomaterials. 1999 Sep;20(18):1727–1741.
[52] Mathew M, Schroeder LW, Dickens B, et al. The crystal structure of α-Ca3(PO4)2. Acta Crystallographica Section B Structural Crystallography and Crystal Chemistry. 1977;33(5):1325–1333.
[53] Yashima M, Sakai A, Kamiyama T, et al. Crystal structure analysis of β-tricalcium phosphate Ca3(PO4)2 by neutron powder diffraction. J Solid State Chem. 2003 2003 November 01;175(2):272–277.
[54] Duncan J, Hayakawa S, Osaka A, et al. Furthering the understanding of silicate-substitution in alpha-tricalcium phosphate: an X-ray diffraction, X-ray fluorescence and solid-state nuclear magnetic resonance study. Acta Biomater. 2014 Mar;10(3):1443–1450.
[55] Szurkowska K, Szeleszczuk L, Kolmas J. Effects of synthesis conditions on the formation of Si-substituted alpha tricalcium phosphates. Int J Mol Sci. 2020 Dec 1;21(23):9164.
[56] Jodati H, Yılmaz B, Evis Z. A review of bioceramic porous scaffolds for hard tissue applications: effects of structural features. Ceram Int. 2020;46(10):15725–15739.
[57] Lu JX, Flautre B, Anselme K, et al. Role of interconnections in porous bioceramics on bone recolonization in vitro and in vivo. J Mater Sci Mater Med. 1999 Feb;10(2):111–120.
[58] Gerhardt L-C, Boccaccini AR. Bioactive glass and glass-ceramic scaffolds for bone tissue engineering. Materials. 2010;3(7):3867–3910.
[59] Woodard JR, Hilldore AJ, Lan SK, et al. The mechanical properties and osteoconductivity of hydroxyapatite bone scaffolds with multi-scale porosity. Biomaterials. 2007 Jan;28(1):45–54.
[60] Shao H, Liang K, Zhou F, et al. Microstructure and mechanical properties of MgO–Al2O3–SiO2–TiO2 glass–ceramics. Mater Res Bull. 2005;40(3):499–506.
[61] Ansari S, Varghese JM, Dayas KR. Polydimethyl siloxane-cristobalite composite adhesive system for aerospace applications. ?Polym Adv Technol. 2009 May;20(5):459–465.
[62] Li X, Rao F, Song S, et al. Effect of cristobalite on the mechanical behaviour of metakaolin-based geopolymer in artificial seawater. Adv Appl Ceram. 2019;119(1):29–36.

[63] Bellucci D, Sola A, Cannillo V. Hydroxyapatite and tricalcium phosphate composites with bioactive glass as second phase: state of the art and current applications. J Biomed Mater Res A. 2016 Apr;104 (4):1030–1056.
[64] Oktar FN, Göller G. Sintering effects on mechanical properties of glass-reinforced hydroxyapatite composites. Ceram Int. 2002;28(6):617–621.
[65] Kader Bashah NS, Sahid S, Sabudin S, et al. Effect of silica in calcium phosphate material for biomedical application. J Teknologi. 2015 December 13;77(25). DOI:10.11113/jt.v77.6760.
[66] Bashah NSK, Noor AFM. The influence of silicon addition in modulation of HA/TCP ratio in biphasic calcium phosphate. Mater Today Proc. 2019;16: 1796–1803.
[67] Jia ZQ, Guo ZX, Chen F, et al. Microstructure, phase compositions and in vitro evaluation of freeze casting hydroxyapatite-silica scaffolds. Ceram Int. 2018 Mar;44 (4):3636–3643.
[68] Tuck L, Astala R, Reid JW, et al. Dissolution and re-crystallization processes in multiphase silicon stabilized tricalcium phosphate. J Mater Sci Mater Med. 2008 Feb;19(2):917–927.
[69] Porter AE. Nanoscale characterization of the interface between bone and hydroxyapatite implants and the effect of silicon on bone apposition. Micron. 2006;37 (8):681–688.
[70] Vandiver J, Dean D, Patel N, et al. Silicon addition to hydroxyapatite increases nanoscale electrostatic, van der Waals, and adhesive interactions. J Biomed Mater Res A. 2006 Aug;78(2):352–363.
[71] Zhang F, Chang J, Lin K, et al. Preparation, mechanical properties and in vitro degradability of wollastonite/ tricalcium phosphate macroporous scaffolds from nanocomposite powders. J Mater Sci Mater Med. 2008 Jan;19(1):167–173.
[72] De Aza PN, Guitian F, De Aza S. Bioactivity of wollastonite ceramics: in vitro evaluation.Scr Metall Mater. 1994 1994 October 15;31(8):1001–1005.